Title

Experimental and computational investigation of confined laser-induced breakdown spectroscopy

Authors

Wang, Y
Yuan, H
Fu, Y
et al.

Publication Date

2016-12-01

DOI

10.1016/j.sab.2016.10.015

Spectrochimica Acta Part B 126 (2016) 44–52

Contents lists available at ScienceDirect

Spectrochimica Acta Part B

journal homepage: www.elsevier.com/locate/sab

Experimental and computational investigation of confined laser-induced breakdown spectroscopy

Yun Wang [a,*], Hao Yuan [a], Yangting Fu [b], Zhe Wang [b,*]

[a] *Renewable Energy Resources Lab (RERL), Department of Mechanical and Aerospace Engineering, The University of California, Irvine, CA 92697-3975, United States*
[b] *State Key Lab of Power System, Department of Thermal Engineering, Tsinghua-BP Clean Energy Center, Tsinghua University, Beijing, 100084, PR China*

ARTICLE INFO

Article history:
Received 26 June 2016
17 October 2016
Accepted 17 October 2016
Available online 22 October 2016

Keywords:
Laser-induced breakdown spectroscopy
Computation
Cavity
Shockwave
Plasma

ABSTRACT

This paper presents an experimental and computational study on laser-induced breakdown spectroscopy (LIBS) for both unconfined flat surface and confined cavity cases. An integrated LIBS system is employed to acquire the shockwave and plasma plume images. The computational model consists of the mass, momentum, and energy conservation equations, which are necessary to describe shockwave behaviors. The numerical predictions are validated against shadowgraphic images in terms of shockwave expansion and reflection. The three-dimensional (3D) shockwave morphology and velocity fields are displayed and discussed.

Published by Elsevier B.V.

1. Introduction

Laser-induced breakdown spectroscopy (LIBS) has been considered as a “future superstar” in analytical chemistry field, with the advantages of fast, in-situ and online analysis, no or minimal sample preparation requirement and the capability of spontaneous multi-element analysis. It is currently encountered with the relatively low sensitivity and repeatability, which hinders its wide commercialization and deployment [1–4]. Spatial confinement offers an effective way to enhance the plasma signal intensity [5–7], and improve the pulse-to-pulse repeatability [8,9]. Various configurations of spatial confinement have been proposed, including the cylindrical cavity [5,6,8,10], hemispherical cavity [11,12] and parallel wall cavity [7,13]. Combined spatial confinement and other physical effects, such as spark discharge in the cylindrical confinement [9] and combined spatial and magnetic confinement [14], were investigated as well.

The current research effort in the spatial confinement was made primarily on the experimental and spectroscopic perspective — using spectroscopic experimental results to clarify the spatial confinement effect [15]. Although there have been discussions on the spatial confinement's impact and reflected shockwave's compressing the expanding plasma [16], effort is still in need to better elucidate their physical nature. It is also very important to know how the plasma and shockwave expand and interact, when is the best time to measure the plasma's spectra, and which part of plasma is most greatly compressed. By understanding the physical behavior of both laser-induced plasma and reflected shockwaves in the spatial confinement, better temporal and spatial resolved techniques can be designed to obtain the spectra with larger intensity and better pulse-to-pulse repeatability.

Numerical modeling of LIBS plasma has always been a hot topic in the field of LIBS as it helps understanding the fundamental physics background and process of LIBS. To date Gornushkin et al. [17–22] have published a few of works in the field, including a free expansion laser-induced plasma model in 1D direction [20], a nonisothermal asymmetric laser-induced plasma model in vacuum [17] and adoption of equations of state on the energy balance instead of ideal gas approximation to model laser-induced plasma [22] etc. Russo et al. [23,24] particularly investigated the laser-induced plasma expansion phenomenon in ambient gas atmosphere using plasma modeling and Hassanein et al. [25] modeled both the laser-induced plasma and the concomitant shockwave on flat surface. However, very little attention has been paid on the plasma and shockwave modeling in cavity or confined cases, which is necessary to understand the physical mechanisms of shockwave-wall and reflected shockwave-plasma interaction, in order to better understand the signal enhancement and stabilization effect by the cavity in LIBS.

In the work, both experimental and computational studies are carried out to capture the shockwaves on a flat surface and in a rectangular groove cavity. The model is implemented in both 2-D and 3-D simulations to predict the shockwave expansion for the two cases, respectively. ICCD fast photography and focused shadowgraph technique were applied to obtain the laser-induced plasma image and shockwave

---

* Corresponding authors.
E-mail addresses: yunw@uci.edu (Y. Wang), zhewang@tsinghua.edu.cn (Z. Wang).

http://dx.doi.org/10.1016/j.sab.2016.10.015
0584-8547/Published by Elsevier B.V.

image in temporal sequence. Direct visual evidence of reflected shockwave compressing the expanding plasma was obtained experimentally.

2. Experimental setup

The experimental setup has been described in our previous work [26]. The laser-induced plasma images were captured by an integrated LIBS system (Applied Spectra, USA). We employed a Q-switched Nd:YAG laser (Quantel, France) with a wavelength of 1064 nm, a pulse width of 8 ns, and a spot size of around 60 μm in diameter. The plasma plume images were captured by an ICCD camera (Andor, UK) under different ICCD settings, including the gate widths, gains, pre-amplifier gains and optical filter types, to obtain the images with optimal image quality at different delay times [26]. The shockwave images were captured separately using another integrated LIBS system (Applied Spectra, USA) with the plasma produced using a Q-switched Nd:YAG laser (Beamtech, China) with a wavelength of 1064 nm and pulse width of 8 ns. Another Q-switched Nd:YAG laser (Quantel, France) with a 532 nm wavelength and 500 ps pulse width serves as the probe laser providing the light source to the shadowgraph formation. The ablation laser pulse energy for each shot in both setups was controlled as 30 mJ/pulse.

The used cubic brass samples are $2 \times 2 \times 2\ \mathrm{cm}^3$ for both flat surface and grooved-channel confinement cases. For the flat-surface testing, the laser pulses were directly shot on the sample surface. For the cavity experiment, one surface of the brass sample was grooved with a straight channel of 3 mm width and 4 mm depth, see Fig. 1. Laser pulses were shot on the centerline of the groove. The samples were mounted on a 3-dimensional control platform when testing. The ICCD and shadowgraph settings in the two cases are identical.

3. Modeling

For the model to be presented in the below section, we exclude the ablation process and choose the initial state of plasma plume at 100 ns after the ablation. The model is targeted at the shockwave behaviors and interaction with the grooved-channel wall. In the flat-surface case, the problem is essentially axisymmetric, thus we chose a 2-D case, see Fig. 2. For the grooved-channel case, it is essentially a 3-D problem. Due to symmetry, the chosen computational domain is a quarter of the grooved channel.

3.1. Governing equations

The governing equations consist of compressible fluid motion and energy conservation, written as [25]:

$$\frac{\partial \rho}{\partial t} + \nabla \cdot \left(\rho \vec{v}\right) = 0 \tag{1}$$

$$\frac{\partial \rho \vec{v}}{\partial t} + \nabla \cdot \left(\rho \vec{v} \vec{v}\right) = -\nabla p - \nabla \cdot \vec{\vec{\tau}} + \rho \vec{g} \tag{2}$$

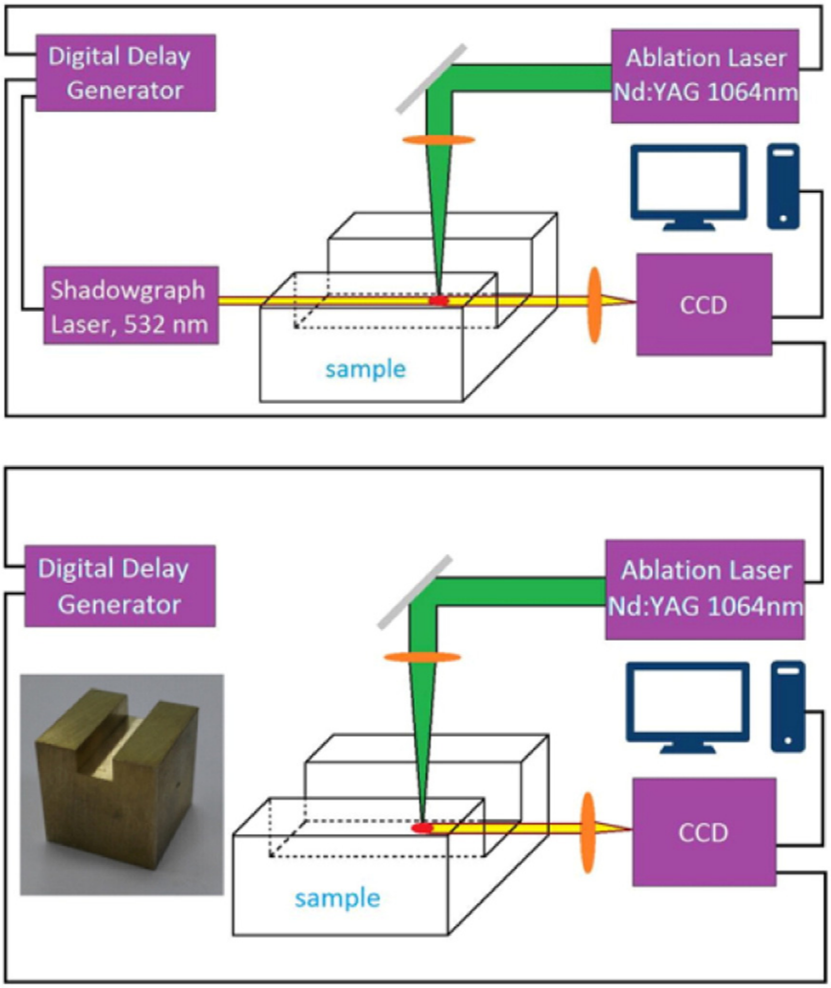

Fig. 1. Diagrams of experimental set-up. (a) shadowgraph set-up for the shockwave images, and (b) ICCD set-up for the plasma plume images. [26].

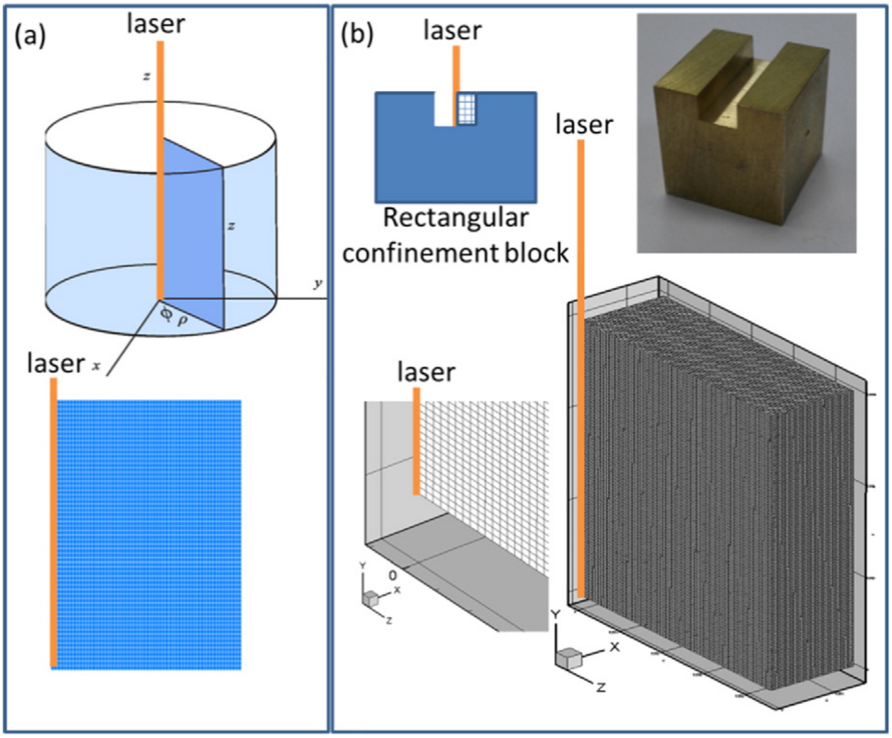

Fig. 2. Computational domains of: (a) the flat surface case (2-D cylindrical coordinate); and (b) the grooved channel case (3-D Cartesian coordinate).

$$\frac{\partial \rho E}{\partial t}+\nabla\cdot\left(\rho\vec{v}E\right)=\nabla\cdot(k\nabla T)-\nabla\cdot\left[\vec{v}\cdot\vec{\vec{\tau}}\right]-\nabla\cdot\left[\vec{v}P\right] \tag{3}$$

where ρ is the fluid density, $\vec{v}$ the velocity vector, E the total energy, p the pressure, $\vec{\vec{\tau}}$ the viscous stress tensor, T the temperature, and k the thermal conductivity. The continuity equation Eq. (1) describes the conservation of mass. Eqs. (2) and (3) describe the conservations of momentum and energy, respectively. In Eq. (3), the three terms on the right represent the condutive effect, heating associated with viscosity, and heating associated with compression and pressure, respectively. We neglect the radiative heat loss and energy flow due to diffusive mass transfer because of the short period of the shockwave event (within a few milli-seconds) and large velocity encountered. In addition, the ideal gas law applies:

$$p=\rho RT \tag{4}$$

where R is the gas constant. The total specific energy E is calculated by:

$$E=e+\frac{\vec{v}^2}{2} \tag{5}$$

The specific internal energy e is a function of temperature only for ideal gases, given by:

$$e=(\gamma-1)RT \tag{6}$$

where γ is the ratio of specific heats at constant pressure and volume.

3.2. Boundary and initial conditions

The computational domains consist of three types of boundaries, including the wall, far field, and symmetry, see Fig. 2. Eqs. (1)–(3) form a complete set of governing equations with three unknowns: $\vec{v}$, P and T. Their corresponding boundary conditions are briefly described as follows:

Far field boundary: Fully developed or no-flux conditions apply.

Walls: No-slip and impermeable velocity conditions are imposed with fixed temperature:

$$T=T_{wall} \tag{7}$$

Symmetry: Symmetric conditions are imposed, including impermeable velocity and no-flux conditions.

For the initial condition, we assume the plasma plume formed around the laser spot center with a radius of 250 μm and a depth of 100 μm. The initial temperature and pressure of the plasma plume are set 10 eV and 200 MPa, respectively. The background gas is air under 1 atm and room temperature 293.15 K. The plasma and background gas are treated as ideal gases, thus their densities are calculated using the equation of state for ideal gases.

3.3. Numerical implementation

The governing equations, Eqs. (1)–(3) , along with their boundary conditions, are discretized using the finite volume method and SIMPLE (semi-implicit pressure linked equation) algorithm [27]. The SIMPLE algorithm updates the pressure and velocity fields from the solution of the pressure correction equation. For the finite-volume discretization, it is convenient to unify all the governing equations, including the transient terms, in the following form:

$$\nabla\cdot\vec{\Gamma}(\Theta)=S_\Theta \tag{8}$$

where Θ stands for any dependent variable in Eqs. (1)–(3) . Integrating the above equation throughout an arbitrary volume V bounded by a closed surface S yields:

$$\oint_S \vec{\Gamma}(\Theta)\cdot d\vec{S}=\int_V S_\Theta dv \tag{9}$$

Table 1
Physical, geometrical, and model parameters.

Description	Unit	Value
Cubic Brass Sample's Dimension	cm^3	2×2×2
Grooved Channel (Cavity) Dimension	mm^3	20(L) ×3(W) ×4(D)
Ambient Temperature	°C	20
Cubic Brass Temperature (T_{wall})	°C	20
Ambient Pressure	atm	1
Ablation Laser Pulse Energy	mJ/pulse	30
Plasma Plume Initial Dimension	μm	250(R) ×100(D)
Plasma Plume Initial Temperature	eV	10
Plasma Plume Initial Pressure	MPa	200
2D Domain Dimension	mm	5×5
3D Domain Dimension	mm	4(L) ×1.5(W) ×4(D)

where $\vec{S}$ is the surface vector. Taking V and S to be the volume V_p and discrete faces S_j of a computational cell, one can reach:

$$\sum_j \int_{S_j} \vec{\Gamma}(\Theta) \cdot d\vec{S} = \int_{V_p} S_\Theta dv \tag{10}$$

The final form of the discrete finite volume equation is then expressed as:

$$B_p\Theta_p^n = \sum_m B_m\Theta_m^n + B\left(\Theta_p^0\right) \tag{11}$$

The above equation is solved by the algebraic multi-grid (AMG) method. The 2nd order of upwind scheme was applied for the advection term. Following the solution of the flow field, the energy is solved. The code is based on the CFD solver we developed for simulating electrochemical flow systems [28,29] and incorporates numerical methods (e.g. the 2nd-order upwind scheme for the advection term) for the shockwave capture. The computational meshes of the flat plate surface (a 2-D case) and cavity (a 3-D case) are shown in Fig. 2. Totally 500 × 500 and 100 × 400 × 400 gridpoints are adopted for the 2-D and 3-D cases, respectively. The geometrical and operating parameters are listed in Table 1. In all the simulations to be presented in the next section, the equation residuals are smaller than 10^{-7}. Adaptive time stepping is used in which the current time step is inversely proportional to the temporal gradient of maximum at the previous time step with the maximum of 1 ns. The 2-D case takes less than 4 h on an Intel® Xeon™ Processor 2.0 GHz; and the 3-D computation typically takes nearly 20 h on a Quad AMD Opteron 6174 4 × 2.20GHz and 64.0 GB DDR RAM.

4. Results and discussion

4.1. Flat surface case

Fig. 3 presents the expanding plasma generated shockwaves at typical time instants. At the early stage, the shockwave (e.g. 100 ns) exhibits a shape stretched in the laser incidence direction, which is primarily caused by plasma eruption. In addition, the theory of laser supported detonation wave (LSD wave) [30] indicates that the energy from the trailing laser pulse increases the temperature and electron density at the shockwave tip, contributing to the non-uniform heating of the shockwave and the observed stretched shape [25]. After the laser energy vanishes, the shockwave exhibit a more hemispherical shape with a radius that can be estimated by the classic Taylor–Sedov theory [31]:

$$R = \xi\left(\frac{E}{\rho}\right)^{1/n+2} t^{2/n+2} \tag{12}$$

where t is the delay time from the initiation of laser illumination, ρ the surrounding gas density, E the energy released during the explosion

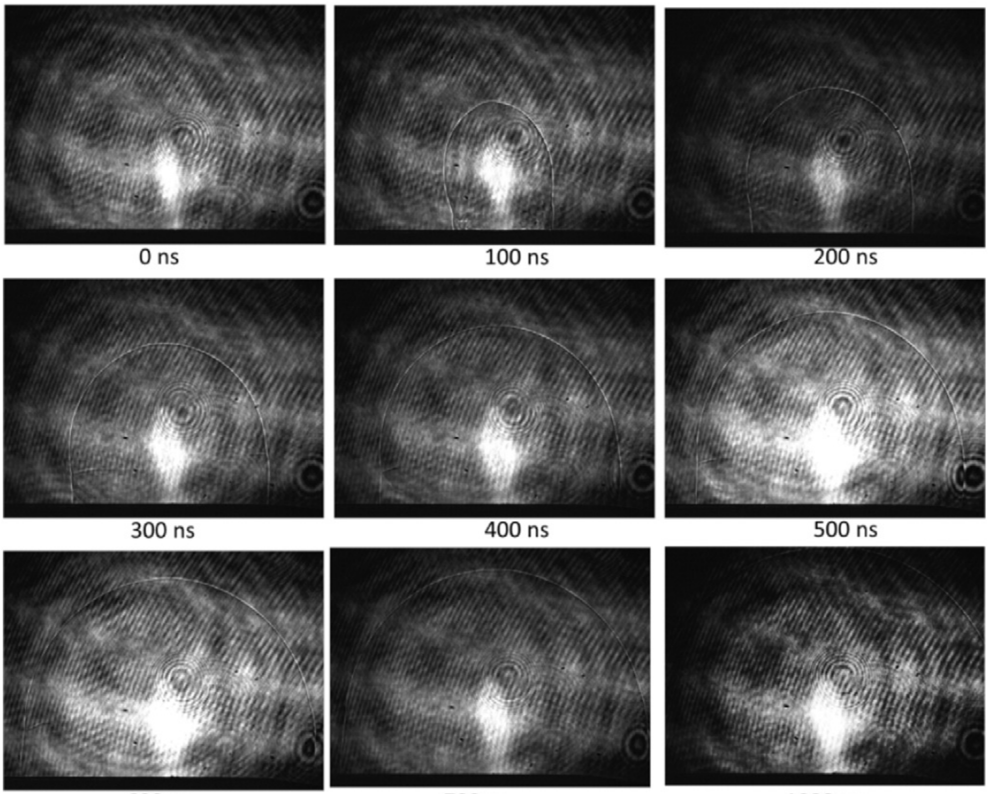

Fig. 3. Evolution of the shockwaves in the flat surface case.

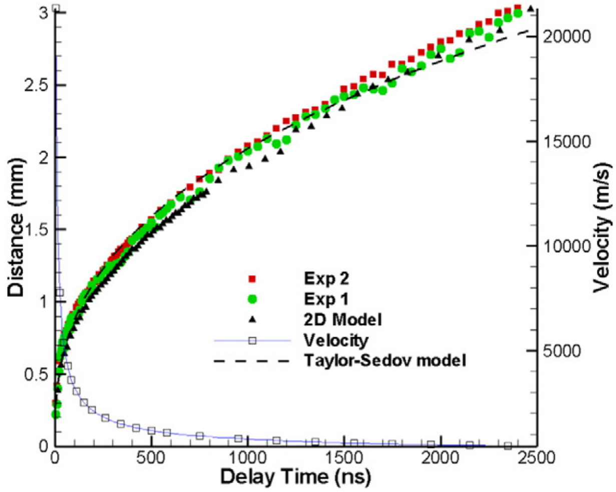

Fig. 4. Comparison of positon-time plots of shockwaves obtained from shadowgraph, Taylor–Sedov model, and 2-D numerical simulation for the plate surface case. The shockwave expansion speed (from Exp 2) is also plotted.

process, and ξ a constant determined by the specific heat capacity ratio. For spherical shockwaves, n is equal to 3, yielding $R \sim t^{0.4}$. Fig. 4 plots the spherical shockwave radii as a function of the delay time measured from the shadowgraphic images in two independent experiments, in comparison with both the Taylor–Sedov model and the 2-D numerical simulation predictions. All the sets of data agree very well. In addition, the radii evolution clearly shows a decreasing trend of the expansion speed with time elapse, as also ploted in the figure.

4.2. Grooved channel confinement

Fig. 5 displays the shockwave expansion and reflection in the rectangular grooved cavity. Prior to reaching the grooved-channel sidewalls, the shockwave behaves similarly as that for the previous flat surface case. The spherical shockwave reached the channel wall at ~700 ns from the laser initiation. When touching the wall, the shockwave was immediately reflected, while the rest continues propagating upward. The reflected shockwave propagating velocity was also evaluated, which is in the same order of magnitude as the nonreflected shockwave. When meeting with the nonreflected one, the reflected shockwave merge with it only in the region near the reflecting wall. The “rings” in the shadowgraph images are due to the diffraction from the dusts on the optical lens.

Fig. 6 presents the validation of 3-D numerical simulation, showing a good agreement for all the instants except 100 ns. The shockwave's location was directly obtained from the shadowgraphic images. The pressure contours in the simulation prediction are shown, with the shadowgraphic data superposed. Physically, the shockwave represents a sharp discontinuity, thus in the numerical solution a largest pressure gradient appears across the shockwave. It is clearly shown that the 3-D simulation prediction captures the time the shockwave hit the channel wall, the upper shockwave movement, the merge area of the reflected and nonreflected shockwaves, and the reflected shockwave shape. As to the initial shockwave (i.e. 100 ns), the nonuniform heating of laser on the shockwave was excluded in the model, thus the stretched shape was not well captured.

Fig. 7 presents the numerically predicted 3-D evolution of the shockwaves. The left plane represents a channel sidewall, the planes (0, y, z) and (x, 0, z) are the symmetric planes; and the below plane (x, z, 0) is the channel bottom wall. It is shown that the predicted shockwave is hemispherical initially (e.g. 400 ns). When hitting the sidewall, the shockwave reflected back, while the rest shockwave remains its original shape. In some plots, e.g. 1500 ns, the merge between the reflected and original shockwave is clearly visible, as seen the projected curve of the merged shockwave on the bottom wall.

Fig. 8 displays the velocity field evolution for the channel cavity case at the plane (x, 0, z). It shows that before the shockwave hit the sidewall the velocity field uniformly points outwards from the laser-hitting spot and pushes the shockwave forward. The velocity is at the order of

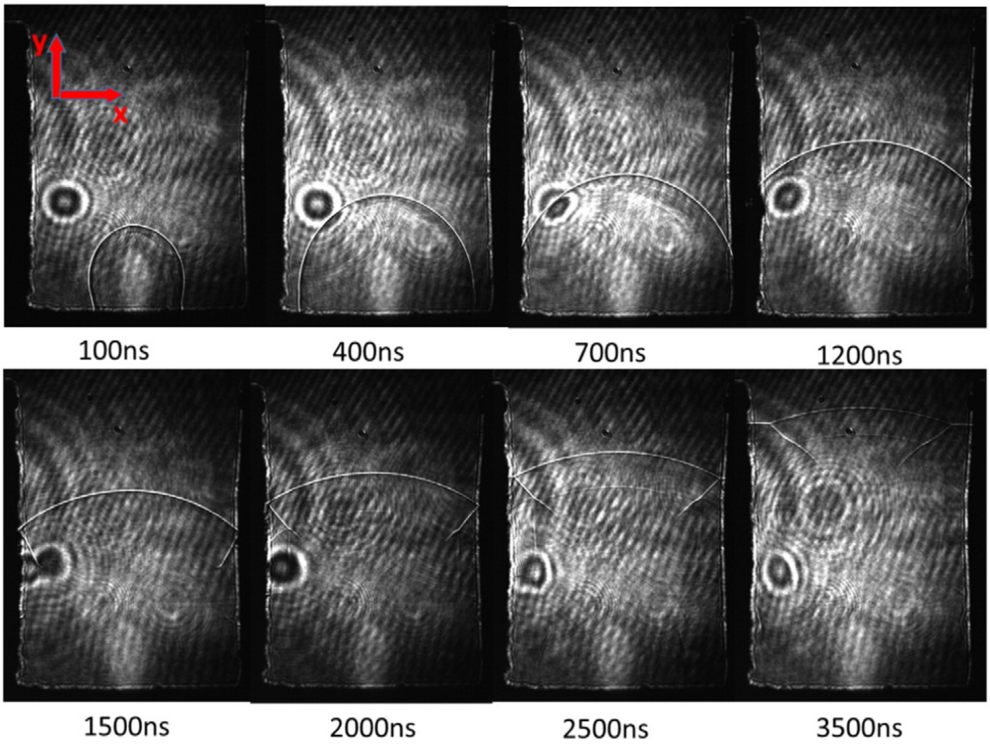

Fig. 5. Evolution of the shockwave in the grooved channel case. The first two plots, i.e. 100 ns and 400 ns, are in different length scales with the rest.

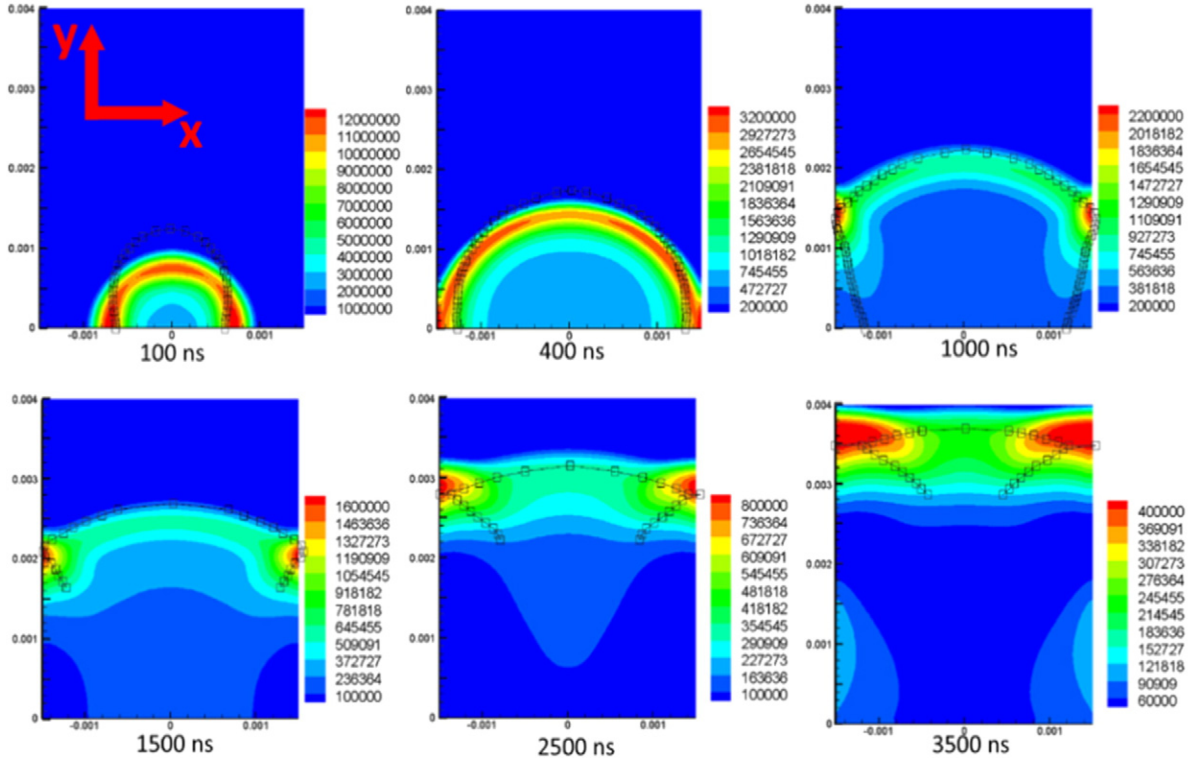

Fig. 6. Shockwave expansion and reflection, captured by the 3-D numerical prediction and shadowgraphic images (the symbol). The contours are the pressure distribution with the unit [Pa].

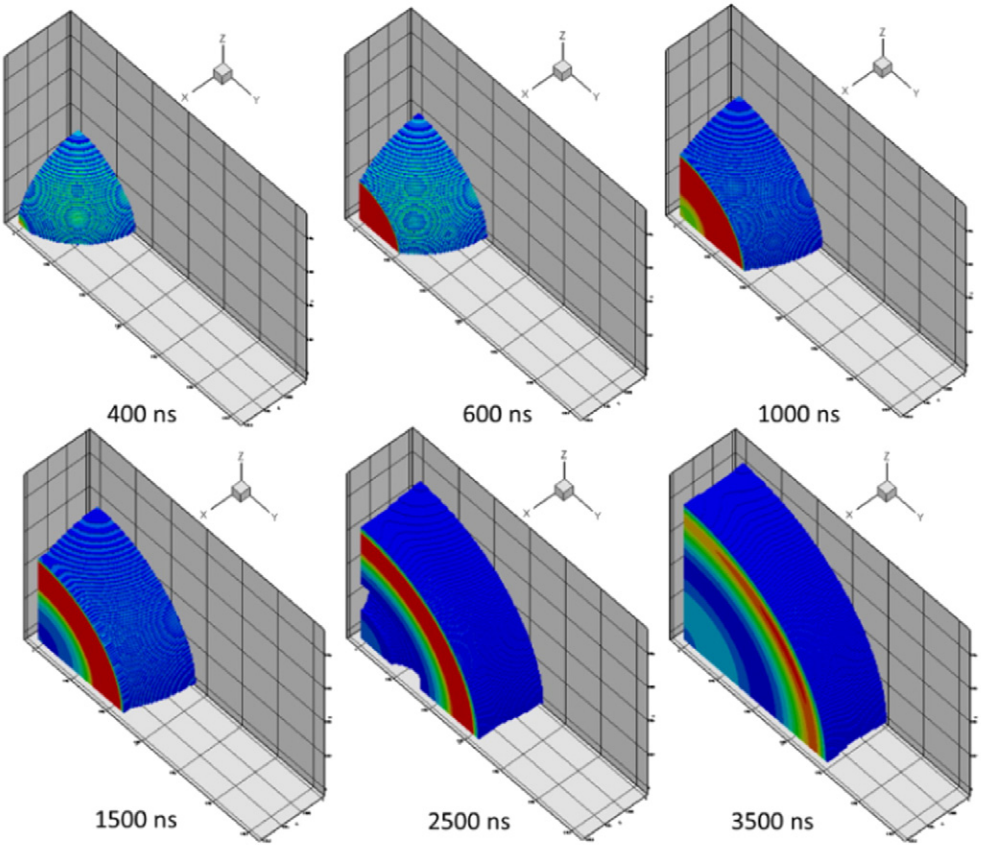

Fig. 7. Shockwave expansion and reflection in the grooved channel case predicted by the 3-D numerical modeling.

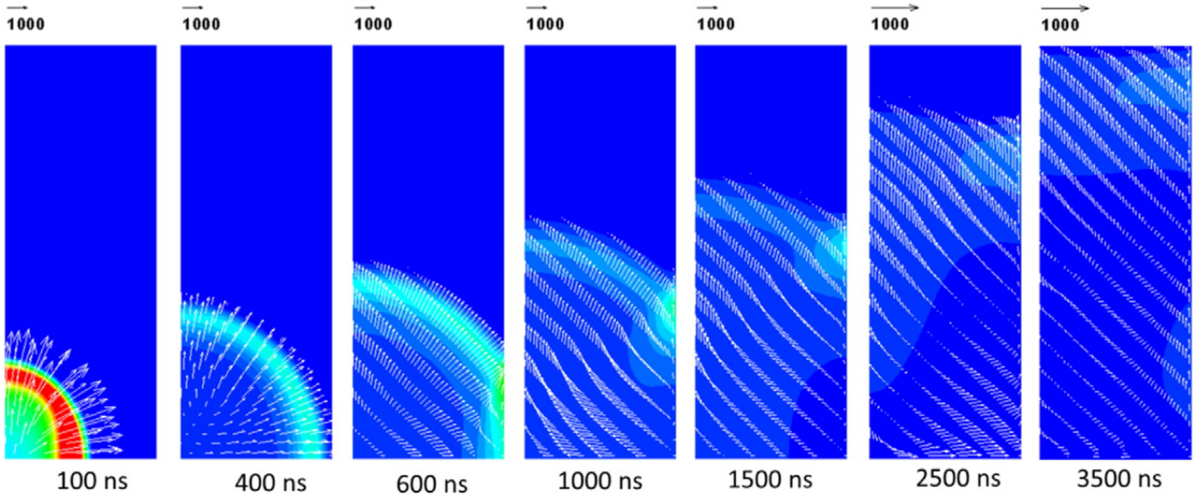

Fig. 8. Velocity field distributions at the plane (x,0,z) for the grooved channel case, predicted by the 3-D simulation. The background contours are pressure distribution, indicating the shockwave location.

1000 m/s at the initial stage (e.g. 100 ns and 400 ns); and decreases quickly, consistent with the expansion speed in Fig. 4. The initial large velocity is promoted by the large amount of laser energy and consequent plasma expansion. When the shockwave hits the sidewall and is reflected, local velocity changes abruptly: at 600 ns, the velocity is rapidly reduced to around 0 near the shockwave-wall region. Fluid flows into the shockwave-wall region to raise local pressure. At 1000 and 1500 ns, it is clear that two regions are visible: one is a strong flow towards the center of the plasma from the reflecting sidewall, which is primarily in the region adjacent to the bottom wall; the other is the strong flow upward pushing the upper shockwave. The transition zone between the two flow regions roughly represents the reflected shockwave location near the reflecting sidewall. At 2500 and 3500 ns, the two regions are still visible, but both regions show outward flows.

4.3. Plasma plume

Similar to shockwaves, the plasma plume expansion behaves similarly as that in the flat surface case at the initial stage (e.g. 100 ns), as shown in Fig. 9. Even before the reflected shockwave front reaches the plasma plume, the plumes exhibit similarly (see 1000 ns) or no shockwave compression effect is visible, seeing (b) 1000 ns. The compression effect by the reflected shockwave is evident at 1800 ns, in which the lower plume was squeezed and the upper plume moves faster upward. From Fig. 5, it is qualitatively seen that the reflected shockwave reaches the lower plume location, indicative of shockwave compression. The compression effect becomes remarkable for latter stage, e.g. 2500 and 3500 ns in (b), in which the plasma plume is further stretched in the vertical dimension and confined in a smaller region than the flat surface case. The modeling results help us better understand the behaviors of the expanding shockwave and plasma and their interactions. As shown in Figs. 6-8, after the shockwave reaches the cavity wall and gets reflected from the cavity wall, the high pressure shock front region containing ambient air moleculars with high kinetic energy compresses the expanding plasma, leading to a more dense and stable hot core of the plasma. This has been demonstrated in our early work [26], see Fig. 10, that during the reflected shockwave-plasma interaction, the plasma emission intensity is significantly higher than that on the flat surface. Moreover, the core position will be regulated by the reflected shockwave to a more stable position, which allows us to find an optimal signal collection angle [26]. In the future work, we will model the interactions between the reflected shockwave and plasma to elucidate the plasma emission enhancement and core position stabilization as observed in the previous experiments.

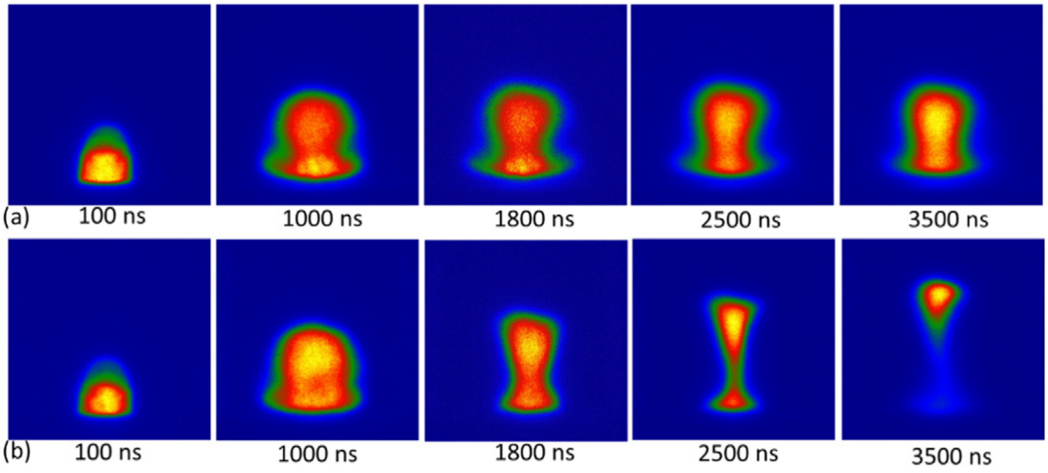

Fig. 9. Evolution of plasma in (a) the flat surface case and (b) cavity confinement case, obtained from the ICCD images. The plasma compression effect was observed after 1800 ns.

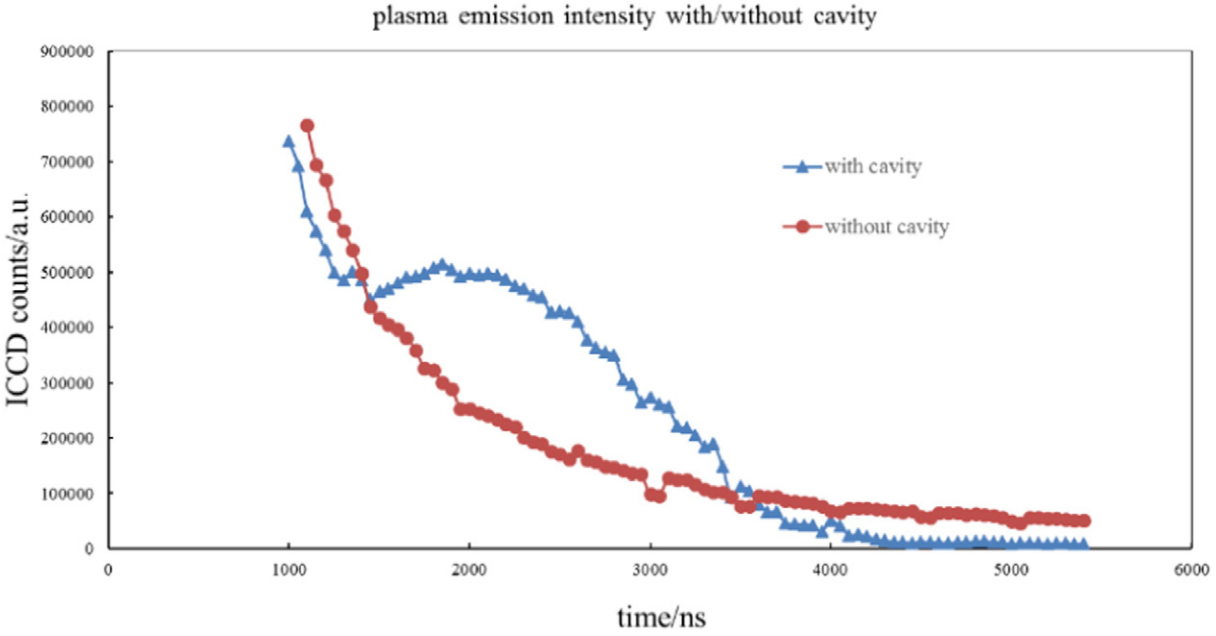

Fig. 10. Plasma emission intensity evolution from the cavity case and the flat surface case [26].

5. Conclusions

In this work, both experimental and computational studies were carried out to investigate the expansion dynamics of shockwaves in both flat surface and channel cavity cases. The computational model was successfully developed and implemented for 2-D (the cylindrical coordinate) and 3-D (the Cartesian coordinate) numerical simulations of the two cases, respectively. The model was validated against experimental results in terms of shockwave propagation and reflection. In the flat surface case, the shockwave expanded into an unconfined space, exhibiting a hemispherical shape specially at the latter stage of expansion. When the channel confinement is present, the shadowgraph images clearly showed that the shockwaves were reflected from the channel sidewall, and the ICCD images indicated that the reflected shockwaves compress the plasma plume, leading a vertical stretch of the plume. 3-D simulation results predict the shockwave shapes, including the merge of the reflected and nonreflected shockwaves. The velocity fields were displayed, showing that a large velocity was promoted initially and push the shockwave expansion. When the shockwave hit the sidewall, local velocity decreased to around zero near the shockwave-wall area. After shockwaves were reflected, two regions were clearly shown in a certain period with one flowing towards the plasma center and the other continuing pushing the upper shockwave. Future work will incorporate the plasma transport equation to the present 3-D model framework, improve the fundamental understanding of the reflected shockwave-plasma interaction, and reveal the impacts of confinement geometry on the plasma enhancement.

Acknowledgement

The authors are grateful for the financial supports from National Science Foundation (CBET-1336873), National Natural Science Foundation of China (No. 51276100, No. 61675110) and the National Basic Research Program (973 Program) of China (No. 2013CB228501).

References

[1] D.W. Hahn, N. Omenetto, Laser-induced breakdown spectroscopy (LIBS), part I: review of basic diagnostics and plasma-particle interactions: still-challenging issues within the analytical plasma community, Appl. Spectrosc. 64 (2010) 335A–366A.
[2] D.W. Hahn, N. Omenetto, Laser-induced breakdown spectroscopy (LIBS), part II: review of instrumental and methodological approaches to material analysis and applications to different fields, Appl. Spectrosc. 66 (2012) 347–419.
[3] Z. Wang, T.-B. Yuan, Z.-Y. Hou, W.-D. Zhou, J.-D. Lu, H.-B. Ding, X.-Y. Zeng, Laser-induced breakdown spectroscopy in China, Front. Phys. 9 (2014) 419–438.
[4] J. Yu, R. Zheng, Laser-induced plasma and laser-induced breakdown spectroscopy (LIBS) in China: the challenge and the opportunity, Front. Phys. 7 (2012) 647–648.
[5] A.M. Popov, F. Colao, R. Fantoni, Enhancement of LIBS signal by spatially confining the laser-induced plasma, J. Anal. At. Spectrom. 24 (2009) 602–604.
[6] A.M. Popov, F. Colao, R. Fantoni, Spatial confinement of laser-induced plasma to enhance LIBS sensitivity for trace elements determination in soils, J. Anal. At. Spectrom. 25 (2010) 837–848.
[7] X. Shen, J. Sun, H. Ling, Y. Lu, Spatial confinement effects in laser-induced breakdown spectroscopy, Appl. Phys. Lett. 91 (2007) 081501.
[8] Z.Y. Hou, Z. Wang, J.M. Liu, W.D. Ni, Z. Li, Signal quality improvement using cylindrical confinement for laser induced breakdown spectroscopy, Opt. Express 21 (2013) 15974–15979.
[9] Z.Y. Hou, Z. Wang, J.M. Liu, W.D. Ni, Z. Li, Combination of cylindrical confinement and spark discharge for signal improvement using laser induced breakdown spectroscopy, Opt. Express 22 (2014) 12909–12914.
[10] X. Shen, J. Sun, H. Ling, Y. Lu, Spectroscopic study of laser-induced Al plasmas with cylindrical confinement, J. Appl. Phys. 102 (2007) 093301.
[11] L.B. Guo, Z.Q. Hao, M. Shen, W. Xiong, X.N. He, Z.Q. Xie, M. Gao, X.Y. Li, X.Y. Zeng, Y.F. Lu, Accuracy improvement of quantitative analysis by spatial confinement in laser-induced breakdown spectroscopy, Opt. Express 21 (2013) 18188–18195.
[12] H.L. Yin, Z.Y. Hou, T.B. Yuan, Z. Wang, W.D. Ni, Z. Li, Application of spatial confinement for gas analysis using laser-induced breakdown spectroscopy to improve signal stability, J. Anal. At. Spectrom. 30 (2015) 922–928.
[13] P. Yeates, E.T. Kennedy, Spectroscopic, imaging, and probe diagnostics of laser plasma plumes expanding between confining surfaces, J. Appl. Physiol. 108 (2010).
[14] L.B. Guo, W. Hu, B.Y. Zhang, X.N. He, C.M. Li, Y.S. Zhou, Z.X. Cai, X.Y. Zeng, Y.F. Lu, Enhancement of optical emission from laser-induced plasmas by combined spatial and magnetic confinement, Opt. Express 19 (2011) 14067–14075.
[15] X.W. Li, Z. Wang, X.L. Mao, R.E. Russo, Spatially and temporally resolved spectral emission of laser-induced plasmas confined by cylindrical cavities, J. Anal. At. Spectrom. 29 (2014) 2127–2135.
[16] H. Sobral, M. Villagrán-Muniz, R. Navarro-González, A.C. Raga, Temporal evolution of the shock wave and hot core air in laser induced plasma, Appl. Phys. Lett. 77 (2000) 3158–3160.
[17] I. Gornushkin, S. Shabanov, N. Omenetto, J. Winefordner, Nonisothermal asymmetric expansion of laser induced plasmas into vacuum, J. Appl. Phys. 100 (2006) 073304.
[18] I.B. Gornushkin, A.Y. Kazakov, N. Omenetto, B.W. Smith, J.D. Winefordner, Radiation dynamics of post-breakdown laser induced plasma, Spectrochim. Acta B At. Spectrosc. 59 (2004) 401–418.
[19] I.B. Gornushkin, A.Y. Kazakov, N. Omenetto, B.W. Smith, J.D. Winefordner, Experimental verification of a radiative model of laser-induced plasma expanding into vacuum, Spectrochim. Acta B At. Spectrosc. 60 (2005) 215–230.
[20] I.B. Gornushkin, C.L. Stevenson, B.W. Smith, N. Omenetto, J.D. Winefordner, Modeling an inhomogeneous optically thick laser induced plasma: a simplified theoretical approach, Spectrochim. Acta B 56 (2001) 1769–1785.

[21] A.Y. Kazakov, I.B. Gornushkin, N. Omenetto, B.W. Smith, J.D. Winefordner, Radiative model of post-breakdown laser-induced plasma expanding into ambient gas, Appl. Opt. 45 (2006) 2810–2820.
[22] S.V. Shabanov, I.B. Gornushkin, Two-dimensional axisymmetric models of laser induced plasmas relevant to laser induced breakdown spectroscopy, Spectrochim. Acta B At. Spectrosc. 100 (2014) 147–172.
[23] S.-B. Wen, X. Mao, R. Greif, R.E. Russo, Expansion of the laser ablation vapor plume into a background gas. I. Analysis, J. Appl. Phys. 101 (2007) 023114.
[24] S.-B. Wen, X. Mao, R. Greif, R.E. Russo, Laser ablation induced vapor plume expansion into a background gas. II. Experimental analysis, J. Appl. Phys. 101 (2007) 023115.
[25] S. Harilal, G. Miloshevsky, P. Diwakar, N. LaHaye, A. Hassanein, Experimental and computational study of complex shockwave dynamics in laser ablation plumes in argon atmosphere, Phys. Plasmas 19 (2012) 083504 (1994-present).
[26] Y. Fu, Z. Hou, Z. Wang, Physical insights of cavity confinement enhancing effect in laser-induced breakdown spectroscopy, Opt. Express 24 (2016) 3055–3066.
[27] S.V. Patankar, Numerical Heat Transfer and Fluid Flow, Hemisphere Publishing Corp, New York, 1980.
[28] Y. Wang, Modeling of two-phase transport in the diffusion media of polymer electrolyte fuel cells, J. Power Sources 185 (2008) 261–271.
[29] Y. Wang, X.C. Adroher, J. Chen, X.G. Yang, T. Miller, Three-dimensional modeling of hydrogen sorption in metal hydride hydrogen storage beds, J. Power Sources 194 (2009) 997–1006.
[30] L.J. Radziemski, D.A. Cremers, Laser-Induced Plasmas and Applications, Marcel Dekker, Inc, 1989.
[31] Y.B. Zel'dovich, Physics of Shock Waves and High-Temperature Hydrodynamic Phenomena, Courier Corporation, 2002.